



Nanoscale shear cohesion between cement hydrates: The role of water diffusivity under structural and electrostatic confinement

Eduardo Duque-Redondo^{a,b,*}, Enrico Masoero^{b,c}, Hegoi Manzano^d

^a Department of Physical Chemistry, University of the Basque Country UPV/EHU, Aptdo. 664, 48080 Bilbao, Spain

^b School of Engineering, Newcastle University, NE1 7RU Newcastle upon Tyne, UK

^c School of Engineering, Cardiff University, CF24 3AA, Cardiff, UK

^d Department of Physics, University of the Basque Country UPV/EHU, Aptdo. 664, 48080 Bilbao, Spain

ARTICLE INFO

Keywords:

Calcium silicate hydrate
Molecular dynamics
Mechanical properties
Shear strength
Interfacial distance

ABSTRACT

The calcium silicate hydrate (C-S-H) controls most of the final properties of the cement paste, including its mechanical performance. It is agreed that the nanometer-sized building blocks that compose the C-S-H are the origin of the mechanical properties. In this work, we employ atomistic simulations to investigate the relaxation process of C-S-H nanoparticles subjected to shear stress. In particular, we study the stress relaxation by rearrangement of these nanoparticles via sliding adjacent C-S-H layers separated by a variable interfacial distance. The simulations show that the shear strength has its maximum at the bulk interlayer space, called perfect contact interface, and decreases sharply to low values for very short interfacial distances, coinciding with the transition from 2 to 3 water layers and beginning of the water flow. The evolution of the shear strength as a function of the temperature and ionic confinement confirms that the water diffusion controls the shear strength.

1. Introduction

The calcium silicate hydrate (C-S-H) gel is the main component of cement pastes and the main responsible for its cohesion and mechanical performance. From the structural point of view, C-S-H has been described either as a continuous matrix with pores [1] or as an assembly of independent colloidal particles [2]; irrespective of this description, it has been shown that the mechanical behaviour of the C-S-H gel can be well captured using nanogranular models [3,4]. Mechanical stress in the C-S-H gel originates from various processes, including externally applied loads, capillary forces in partially saturated pores, and chemical reactions producing crystallisation pressure. As a result, the C-S-H gel is believed to feature a heterogeneous stress field at the sub-micrometre level, whose relaxation over time controls the viscous behaviour and creep deformations of the materials, which are its main modes of mechanical degradation [5]. Nanoparticle-based simulations have shown that collective rearrangements of multiple C-S-H units at the 10–50 nm scale produce stress relaxation and creep strain that are consistent with the experimental results, also justifying some fundamental hypotheses in macroscale models [6–8]. The triggering of such mesoscale rearrangements is controlled by the interfacial cohesion between adjacent C-S-H nano-units [9–12]. Understanding and even tuning such cohesion

would be key advances toward concretes with nano-engineered strength and durability, creating new opportunities for the design of future, more sustainable, cementitious materials.

The solid nano-units of C-S-H consist of few nm thick platelet-like particles [13]. Their internal structure is generally described as an ill-crystalline layered oxide akin to the inosilicate mineral tobermorite [14] with imperfections, formed by finite silicate chains. The most stable finite silicate chains in C-S-H gel are those that are composed of 3n-1 silicate tetrahedra, with n being an integer number [15]. Thus, the silicates formed dimers (when n = 1), pentamers (when n = 2), and so on. Like other layered oxides [16–19], the interlayer space has a variable thickness and can accommodate a variety of molecules and ions. Under normal conditions, the interlayer space in bulk C-S-H is filled with water molecules and Ca²⁺ ions and has a thickness of ~0.5 nm [20,21]. The tobermorite-like layers are held by strong ionic-covalent forces, compared with the weaker electrostatic interactions between stacked layers. Therefore, the internal structure of the layers is likely to remain stable while adjacent particles slide over each other, concentrating the shear strain in the weaker interlayer spaces. In an extreme simplification, one could then conceptualise adjacent C-S-H particles as rigid blocks separated by a lubricant (water) layer in between.

The interlayer sliding of adjacent C-S-H particles has been suggested as the possible origin of creep in cementitious materials [22,23].

* Corresponding author at: Department of Physical Chemistry, University of the Basque Country UPV/EHU, Aptdo. 664, 48080 Bilbao, Spain.

E-mail address: eduardo.duque@ehu.eus (E. Duque-Redondo).

<https://doi.org/10.1016/j.cemconres.2022.106716>

Received 13 July 2021; Received in revised form 2 December 2021; Accepted 10 January 2022

Available online 18 January 2022

0008-8846/© 2022 The Authors.

Published by Elsevier Ltd.

This is an open access article under the CC BY-NC-ND license

(<http://creativecommons.org/licenses/by-nc-nd/4.0/>).

Abbreviations

C-S-H	Calcium Silicate Hydrate
GSF	Generalized stacking fault
MD	Molecular Dynamics
D	diffusion coefficient

Experimental observations indicate that in presence of deviatoric stress the C-S-H nanoparticles can display preferential orientations, aligning the c-axis of the C-S-H layers with the principal direction of compression [24–26]. These works also highlight the role of interlayer water as a lubricant, finding that water-rich interlayers facilitate the sliding of C-S-H layers and reduce the creep modulus [23,24,26,27]. The resistance to shear deformation was also investigated in tobermorites [28], a clay mineral with a layered structure that resembles that of C-S-H gel. The authors observed that, in all siliceous tobermorites, shear stress is relaxed via the interlayer, by sliding of adjacent silicate layers, as suggested for the C-S-H gel. By contrast, they found that in Al-substituted tobermorites, stress relaxation occurs in the intralayer by the rearrangement of the CaO layer, similar to the relaxation mechanism observed in C-A-S-H [24]. Manzano et al. [10] employed atomistic simulations to compute and compare the shear strength of a bulk model of C-S-H, with a calcium-to-silicon (C/S) molar ratio of 1.65, and that of its crystalline counterpart tobermorite 14 Å. By applying a quasistatic shear strain, they found that the C-S-H gel model was more ductile than its crystalline counterpart, attributing this to the disordered nature of the C-S-H. A similar effect of molecular-scale disorder on shear behaviour has been also found in related materials, such as the geopolymer-zeolite system [29]. Palkovic et al. used both an affine shear deformation and a generalized stacking fault (GSF) method, also in the quasistatic regime, to explore the same C-S-H model as Manzano et al. They confirmed the previous results and proved that the GSF method, usually employed for homogeneous glasses, can also be applied to heterogeneous systems if the slip displacement is applied to an appropriate set of atoms [30]. Morshedifard et al. explored the long-term relaxation of a C-S-H model using a quasistatic cyclic loading method that consisted of a sequence of affine shear displacements followed by enthalpy minimization [9]. As in the previous studies, they found that non-affine strain accumulated in the interlayer water region. To further investigate the effect of water, they increased the water content in the C-S-H model, thus increasing the interlayer space. They found a sharp change in creep compliance (C) regimes at an interfacial distance of ~ 0.1 nm when C changed from having a constant value, attributed to the solid C-S-H, to linearly decreasing with the interfacial distance itself [9].

As the experimental studies, these molecular scale simulations highlighted the key role of interlayer water in the shear behaviour of C-S-H. Assuming nanogranular C-S-H models [3,4,31] and the microscale creep mechanism suggested from experiments [9–12], the same mechanism should govern the long-term relaxation under constant stress, and the temperature must play a pivotal role in the cohesion between C-S-H surfaces. All these previous simulations rely on energy minimisation to relax the atomic stress. However, water mobility in the interlayer space may significantly impact cohesion and shear behaviour. Energy minimization does not allow for temperature-driven fluctuations, whose importance has been recently explored using molecular dynamic simulations on the creep behaviour of C-S-H [32]. The impact of water diffusion and temperature on the shear cohesion of C-S-H is still to be explored.

In this work, we perform non-equilibrium molecular dynamics at room temperature to investigate the effects of water diffusivity and temperature in the interlayer cohesion between adjacent C-S-H layers subjected to shear strain, which cannot be captured by using quasistatic simulation schemes. In particular, we aim to understand the interplay

between the interfacial distance and the shear cohesion in the C-S-H gel as the controlling feature for mesoscale rearrangements prompting the mechanical degradation of cementitious materials. For that purpose, we apply a shear strain rate of 10^8 s^{-1} to the plane perpendicular to the interfacial layer, considering variable interfacial distances, ranging from bulk interfacial space to more than 1 nm. We assume that the tight or perfect contact between particles is equal to the bulk interfacial space, hereinafter called perfect contact interface. We investigate the physico-chemical mechanisms that govern the cohesion between adjacent C-S-H layers, with emphasis on the role of water as a lubricant medium. The simulations reveal that the shear strength is maximum when adjacent C-S-H surfaces are at the perfect contact. The shear strength decreases sharply already at very small interfacial distances, as water becomes able to flow already when forming a trilayer between the adjacent C-S-H. The correspondence between water diffusion and loss of cohesion is also confirmed by looking at the effect of temperature and ionic confinement. Thus, the results indicated that water diffusivity is the key parameter controlling the shear strength and cohesion in the C-S-H gel.

2. Computational models & methods

2.1. Pore model construction

Fig. 1 shows a schematic of the C-S-H gel, made of randomly oriented and aggregated nano-units. The overall mechanical properties of the gel are determined by the cohesion at the interfaces (viz. the contact points) between particles, and Fig. 1 shows two examples where such interfaces may be tightly or loosely connected. The exact structure and composition of interfaces between C-S-H nano-units are not known, owing to the disorder and non-stoichiometric composition of the material. Here we construct model interfaces by considering that their structure is akin to that of the interlayer space in bulk C-S-H. Specifically, we create a range of model interfaces going from perfect contact, which is assumed to be identical to the interlayer space in bulk C-S-H, to progressively looser contacts, modelled by widening the interlayer space and allowing more water in, as the interlayer space is always saturated by water under normal conditions [33,34]. Other imperfect interfaces would certainly be present, for instance, contact regions where C-S-H particles have different orientations [35]. From a quantitative point of view, the water properties and shear strength may be affected by the C-S-H particle orientation due to the greater surface charges on their borders, but qualitatively there will be no major differences. Thus, we expect that the mechanisms of interfacial water diffusion and their impact on cohesion emerging from the model structures in this work will be sufficiently general and relevant to other interfacial morphologies too. It is also interesting to note that the interfacial properties may also influence the particle orientation, agglomeration, and growth processes during the C-S-H gel formation at the larger nano-to-micro mesoscale. Indeed, mesoscale simulations of such processes use effective interaction potentials that can be informed by said interfacial properties [1,36]. However, a direct extrapolation from interfacial properties to meso-structure is not possible at this stage and would require dedicated mesoscale simulations which are beyond the scope of the manuscript.

The initial C-S-H structure, with a composition $\text{C}_{1.65}\text{S}_1\text{H}_{1.5}$, was built following the process described for model 1 in ref. [37]. This procedure results in a disordered tobermorite-like structure similar to that obtained using Pellenq's and Qomi's procedures [38,39], although the procedure used in this work does not generate silicate monomers at high C/S ratios, in the line with experimental findings [40,41]. The C/S ratio in C-S-H gel ranges from 1.2 to 2.1, with the mean value at 1.75 [42], close to the C/S ratio of 1.65 of our model. The final structure is in good agreement with experimental values: it has a mean chain length of 3.1 silicon units [43], a density of $2.35 \text{ g}\cdot\text{cm}^{-3}$ [44], and the average basal spacing is 1.25 nm [14]. The width of the bulk interlayer space is difficult to quantify due to the roughness of the C-S-H surface and the poor structural order of the C-S-H structure [45], yet values of ~ 0.5 nm have been previously

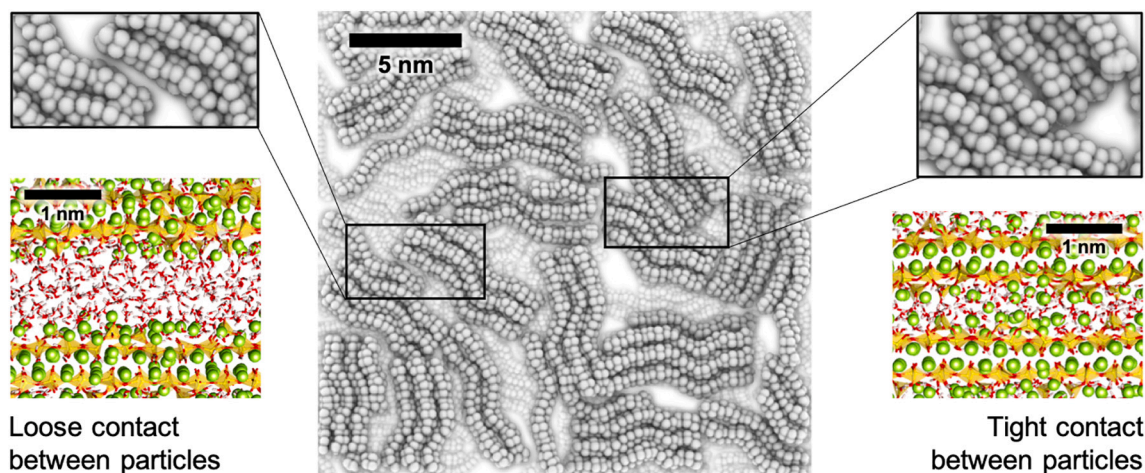


Fig. 1. Schematic picture of the nanoscale structure of the C-S-H gel. The material is made of solid regions or “particles” with layered structures arranged irregularly and creating polydisperse pore spaces. The magnifications show two possible interparticle interfaces: a tight contact one (right), where the interface between regions is equivalent to the bulk (perfect contact) interlayer space (nominal interfacial distance $d = 0$ nm), and a loose contact (left) where there is a wider water-filled gap between adjacent particles (nominal interfacial distance $d = 0.65$ nm). The full simulation box for tight and loose contact can be seen in the Supplementary Information (Fig. 1).

suggested for the perfect contact interface [20,21]. The slit pores, or interfaces, were constructed inserting extra space in the centre of the perfect contact interface, up to 1 nm. The interlayer space was then saturated with water using a space filling algorithm [46], and the system was equilibrated at room temperature and pressure in the isothermal-isobaric ensemble to obtain the actual interfacial distance. The final simulation box dimensions are $4.22 \text{ nm} \times 4.48 \text{ nm}$ in the layers' plane directions (xy plane), whereas the sizes in the perpendicular direction (z direction) range from 5.03 nm for the case with ideal contact to 6.10 nm for the largest interfacial distance. We attributed to the perfect contact interface model, with a z-box size z_0 , a nominal interfacial distance $d = 0$ nm. In this way, when the slit pore is expanded in the z-direction to z_1 and filled with water, the nominal interfacial distance, $z_1 - z_0$, matches the expansion of the bulk interlayer. Then the C-S-H models were equilibrated in the npt ensemble, so the nominal interfacial distance slightly varies, leading to z_2 . Therefore, the results shown in this work are expressed in terms of the equilibrated interfacial distance, i.e. $z_2 - z_0$.

2.2. Computational details

The Molecular Dynamics (MD) simulations were carried out using the ReaxFF empirical force field, as implemented in the LAMMPS code [47]. The Ca/Si/O/H set of parameters developed in refs [48,49] was used, which has been used to build atomistic C-S-H models and has been shown to reproduce accurately the structure, elastic properties, and chemical reactions in calcium silicates [10,39,50–52]. In contrast to other force fields, such as CSH-FF or ClayFF, commonly used for C-S-H gel simulation, ReaxFF is a reactive force and allows the dissociation of water molecules to form hydroxyl groups in the dangling oxygen atoms of the silicate chains. This results in the formation of Si-OH and Ca-OH pairs in such a way that it is not imposed manually on certain surface locations; these OH groups may have considerable implications for the shear response, especially in the tight contact regime. Additionally, ReaxFF has been demonstrated to be well suited to the simulation of disordered structures, like that of C-S-H with a high C/S ratio and it is easy to use since formatted files containing all parameters are available. These parameters are included in the Supplementary Materials and they are also available in *cemff* database (<http://cemff.epfl.ch>). The equilibration of the interface models was carried out at room temperature and pressure until the water density in the interlayer space became constant. This equilibration was run for 1 ns, although typically it took less than 0.25 ns to reach the equilibrium. These simulations were carried out in

the isobaric-isothermal ensemble, using a Noose-Hover thermostat and barostat [53] with coupling constants of 0.02 and 0.2 ps for the temperature and pressure respectively. The equations of motion were integrated using a Verlet algorithm [54] with an integration step of 0.2 fs.

The shear deformations were performed on the equilibrated systems applying a simple shear strain to the plane perpendicular to the interfacial layer (xz plane). We tested several strain rates, from 10^{11} to 10^8 s^{-1} finding that rates greater than 10^9 s^{-1} did not provide enough time for molecules to relax while the deformation was applied, thus leading to an overestimation of corresponding stress: (see Fig. 2). Thus, we applied a strain rate of 10^8 s^{-1} and the shear deformations were done in the canonical (NVT) ensemble, in the same temperature conditions and using the same parameters as described above.

The analysis of the molecular dynamics trajectories was performed using the TRAVIS [55,56] (TRajjectory Analyzer and VISualizer) and OVITO [57] (Open Visualization TOol) programs. A detailed description of the methodologies used by these codes is given in the Supplementary Information (S.I.).

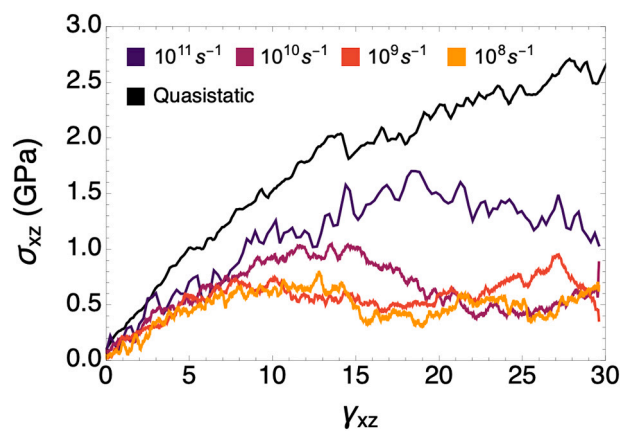


Fig. 2. Stress-strain curves for the perfect contact interface case obtained from non-equilibrium MD at different strain rates, from 10^{11} to 10^8 s^{-1} . The quasistatic case is also shown for comparison.

3. Results and discussion

3.1. Interlayer space characterization

We first analysed the effect of nanoconfinement on the arrangement of water molecules in the interlayer space. The density profiles of water in the perpendicular direction to the interfaces show a relatively ordered structure in the interlayer spaces, see Fig. 3a. In all the cases, there are two small peaks of local water density immediately next to the surfaces. These peaks correspond to water molecules that are strongly attached to the surfaces, due to the presence of surface defects in the molecular structure of C-S-H. Similar surface layers are not observed in other layered materials with regular surfaces, such as clays [58–60]. The density profiles of water molecules confined in the interlayer of a crystalline tobermorite show a similar symmetric distribution, well defined peaks for water populations close to the pairing and bridging silicate groups, as well as other populations further away from the surface as the interlayer spacing increases, but no water population related to surface defects has been observed [60]. Moving toward the centre of the interlayer space, there is a variable number of high density peaks, from 2 to 4, depending on the interfacial distance. The peaks are often split and/or featuring shoulders, which is also due to the irregularity of the solid substrate. A transition between 2 and 3 water layers between the C-S-H surface and centre of the interlayer space takes place at an interfacial distance of approximately 0.3 nm. A transition between 3 and 4 layers occurs approximately at 0.75 nm.

Fig. 3b quantifies the total amount of excess water in the interlayer space. We use the term “excess” because the interlayer space contains some water also in the case of tight contact in Fig. 1, to which we have attributed an interfacial distance of zero. Fig. 3b thus plots the difference between water content at a generic interfacial distance and water content in the tight contact case. The figure shows that excess water content increases linearly with the width of the space itself, viz. the interfacial distance, with small deviations from linearity for the smallest pores. The gradient of the line in Fig. 3b is the number of water molecules per volume, i.e. the average water density in the interlayer space. All this indicates that the average density of water in the interlayer space is constant, as opposed to its local density which features the richer structure in Fig. 3a. The average density of water, from the line gradient in Fig. 3b, is $1.02 \text{ g}\cdot\text{cm}^{-3}$; this value is very close to that of bulk water, indicating that confinement has a minor effect on the average density of water. Previous studies reported a wide range of values for the average density of confined water, from 0.8 to $1.5 \text{ g}\cdot\text{cm}^{-3}$, depending on the force field and the method used to quantify the water density [20,49,52]. The calculation of the density done here should be more accurate than other methods like the Connolly surface [61] or the

Voronoi analysis [62], as the present one is a parameter-free approach that does not require problematic approximations to account, for example, for surface roughness or atomic volumes. However, it is known that the ReaxFF force field underestimates the density of bulk water by about 7%. If this discrepancy in the bulk case is extrapolated to the density in our confined system, the computed density would increase up to $1.09 \text{ g}\cdot\text{cm}^{-3}$.

3.2. Interfacial shear strength

Fig. 4a shows that the shear strength of the ideal (tight contact) interface is approximately 0.72 GPa; this value is significantly greater than the macroscopic shear strength of cement paste, which is in the order of a few MPa only. This well-known discrepancy between atomistic simulations and macroscopic experiments is due to the presence of strength-controlling defects at larger mesoscales in the experimental samples. Fig. 2 showed that the maximum shear stress, viz. the strength, is reached at a shear strain of approximately 12.5%. This strength value is significantly smaller than computed in previous simulations of bulk C-S-H in the literature, which reported strength values between 2 and 3 GPa [10,30,38,49,63]. Besides the different water content of the samples and the procedure chosen to build the C-S-H models, the key difference between our work and previous ones in the literature is that the latter used quasistatic deformation schemes, where entropic effects are not taken into account, whereas we imposed deformations at constant temperature instead of using a quasistatic deformation protocol. Fig. 2 shows indeed that we also predict a strength of 2.7 GPa when using a quasistatic deformation protocol in athermal conditions. Fig. 2 also shows that the shear modulus at finite temperature is approximately half of that from quasistatic simulations. A similar result was obtained for the out-of-plane elastic moduli of clay [64]. However, we argue that simulations at finite temperature are more realistic, and indeed the new values of shear strength in Fig. 4a are more consistent with the cohesion of 0.33 GPa calculated from nanoindentation experiments interpreted with the Drucker-Prager strength model [65].

Fig. 4a also shows that the shear strength declines sharply with the interfacial distance. To investigate this trend, Fig. 4b addresses the mechanisms of stress relaxation during shear deformations in C-S-H. Specifically, the figure shows the spatial distribution of the local shear strain in the C-S-H samples when subjected to an overall average shear strain. The local strain indicates where structural changes are taking place to relax the accumulated stress. For small interfacial distances all the atoms in the structure, both interlayer water and Ca and Si atoms in the solid layers of C-S-H, display significant local deformations and participate in the relaxation mechanism. For larger interfacial distances, stress relaxation is only prompted by deformations in the interlayer

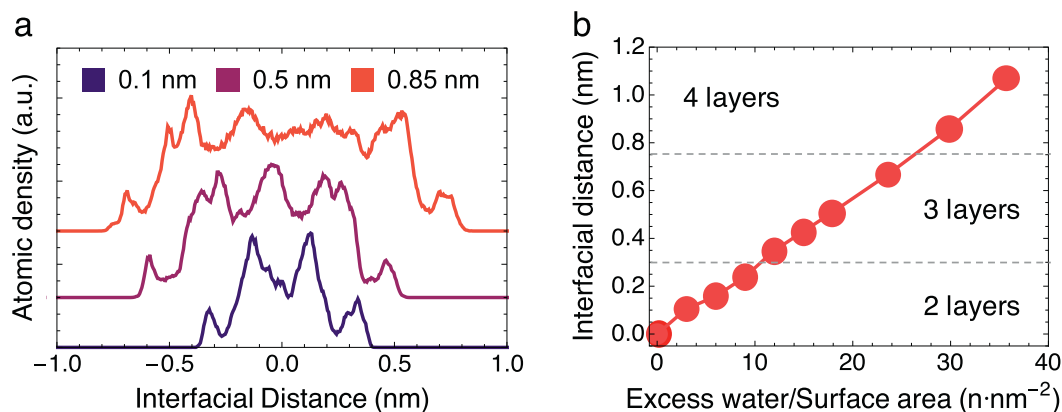


Fig. 3. (a) Water density profiles for selected interfacial distances: 0.1, 0.5 and 0.85 nm. The value 0 nm indicates the middle of the interlayer space. (b) Increase in excess water content per unit surface area as the interfacial distance grows. The horizontal lines divide the plot according to the number of water layers in the perpendicular (z) direction, as indicated by the peaks in (a).

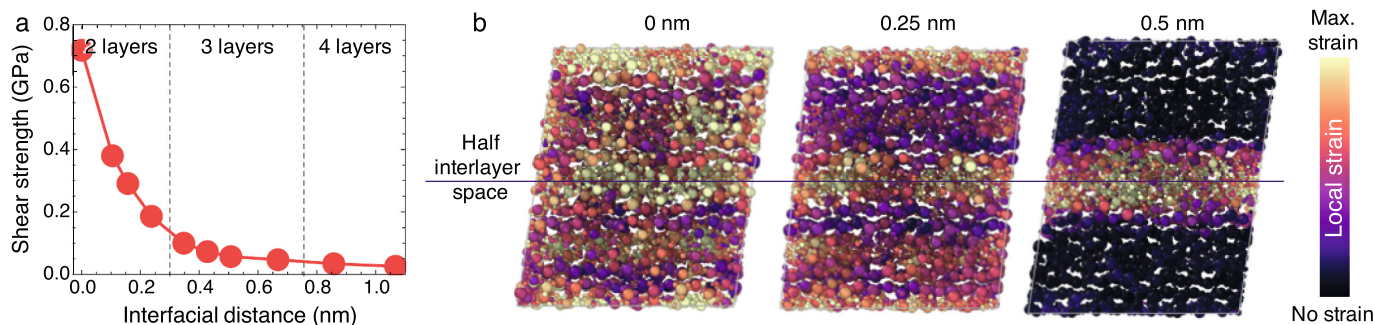


Fig. 4. (a) Evolution of shear strength as a function of interfacial distance; the vertical lines indicate the transitions between the different number of water layers, as in Fig. 3b. (b) Normalized spatial distribution of the local shear strain at 15% average shear strain, for the C-S-H with an interfacial distance of 0 (perfect contact interface), 0.25 and 0.5 nm.

space, where water resides, since the local strain is concentrated in that region, leaving the solid C-S-H layers undeformed. This is because the deformation of the C-S-H layers may imply the distortion or rupture of Si—O covalent bonds of the silicate chains, which require higher energy regarding the cohesive electrostatic and dispersive forces in the interlayer space. As a result, when the interlayer space is sufficiently rich in water, C-S-H relaxation under shear is sustained by layers sliding over each other through this interlayer space, with interfacial distance and water content determining cohesion and mechanical performance under shear. This agrees with the plastic deformations observed by Gardner et al. [24]. Raman spectroscopy experiments revealed that, in non-crosslinked C-S-H samples, as the model analysed in this work, the relaxation mechanism involves the sliding of the silicate chains through the water-rich interlayer. Similar *stick-slip* relaxation mechanisms have already been simulated in C-S-H and other layered materials [10,66–68].

3.3. Water properties

Our results so far have shown that the cohesion between C-S-H layers under shear strain is governed by interfacial distance and water content. Therefore, there should be a water property correlating the sharp drop of the shear strength at short interfacial distances shown in Fig. 4a. A first correlation is with the results on water structure in Fig. 3, in that the loss of cohesion and strength take place approximately at the interfacial distances at which a bilayer of water turns into a trilayer. This correlation with structure, however, does not per se explain the change in mechanical behaviour. Other factors that may link structure with mechanical behaviour are thus explored below, in particular the network of hydrogen bonds and the diffusivity of water in the interlayer space.

Previous works have suggested that the hydrogen bond network might significantly contribute to cohesion in layered composites [68–70]. To examine this possibility, we have computed the average number of hydrogen bonds per water molecule. We considered separately the hydrogen bonds between water molecules and the hydrogen bonds between water molecules and other atoms on the C-S-H surface. Fig. 5a shows that the total (water-water plus water-C-S-H) number of hydrogen bonds per water molecule increases from 1.7 to 2.5 as the interfacial distance increases. At perfect contact (zero interfacial distance) the number of water-water hydrogen bonds is approximately the same as the number of water-C-S-H bonds. Instead, at higher interfacial distances and water content, the contribution of the hydrogen bonds between water molecules becomes dominant, up to representing nearly 90% of the total. This is just a straightforward reflection of the larger number of water molecules in the wider interfaces. Nevertheless, the maximum value is still far from the average number of hydrogen bonds per water molecule in bulk water, which has been computed in 3.5 bonds per molecule [71,72]. This means that the network of hydrogen bonds in the confined space is less developed than in bulk water, despite the confined water having slightly higher density, a situation comparable to that of supercooled water [73]. However, Fig. 5a does not feature any significant change in the number of hydrogen bonds when the bilayer-to-trilayer transition occurs. This indicates that the network of hydrogen bonds does not control the sharp decay in shear strength in Fig. 4a.

Another quantity that might impact the mechanical behaviour is the lifetime of the hydrogen bonds, i.e. the average time that a hydrogen bond persists before breaking and the water molecules reorient to form new hydrogen bonds. Fig. 5b shows the half lifetime of water-water and water-C-S-H hydrogen bonds as functions of the interfacial distance. The

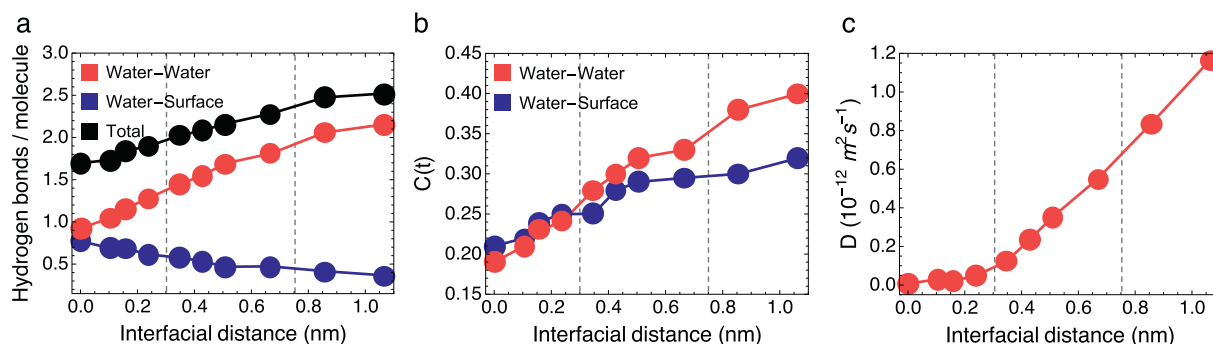


Fig. 5. (a) Average number of hydrogen bonds per water molecule as a function of the interfacial distance: bonds between water molecules are in red, bonds between water molecules and other atoms from the C-S-H surface are in blue, the sum of the two (total) is in black. (b) Hydrogen bond half lifetime as a function of the interfacial distance. Red and blue lines represent the water-water and water-surface contributions. (c) Average diffusion coefficient of water molecules as a function of the interfacial distance. In all subfigures, the vertical lines indicate transitions between different numbers of water layers, as in the previous Fig. 4. (For interpretation of the references to colour in this figure legend, the reader is referred to the web version of this article.)

lifetime of both types of bonds increases with the interfacial distance, going from 0.20 ps to 0.40 ps; this is significantly different from values previously reported in the literature for bulk water, where the average half lifetime ranged between 1.0 ps and 1.2 ps [74,75]. The lifetime of the hydrogen bonds is greater in bulk water because the network of hydrogen bonds is more stable when it features 3.5 bonds per water molecule, as opposed to only 2.5 in the interlayer space here (see Fig. 5a). When there are fewer hydrogen bonds, individual water molecules tend to rotate faster to search for new local configurations and create more hydrogen bonds; this explains the lower lifetime of the hydrogen bonds when there are fewer bonds per molecule. Wider interlayer spaces feature more hydrogen bonds per water molecule (see Fig. 5a) and therefore also the average lifetime of the hydrogen bonds is greater. Nevertheless, no major change occurs at the transition distance of 0.3 nm, therefore the drop in shear strength is not explained by the lifetime of the hydrogen bonds either.

The last mechanism to be considered here and that might impact cohesion is the diffusion of water in the interlayer space. Fig. 5c shows the diffusion coefficient, D , of the water molecules as a function of the interfacial distance. D is calculated as described in the S.I. D is very small when the interfacial distance is below 0.3 nm, but as soon as a trilayer of water is formed (at interfacial distances over 0.3 nm) the diffusion coefficient starts to increase linearly with the interfacial distance. This change in diffusivity at 0.3 nm coincides with the loss of cohesion and decay of the shear strength in Fig. 4a. Our interpretation is that, in a trilayer configuration, the water molecules that are no longer directly coordinated to surface atoms on the C-S-H start to flow, causing the increase in diffusivity as well as the reduction in shear strength. A similar change in diffusivity regimes with the interfacial distance has also been reported for clay, which is also a layered material at the molecular scale [59].

3.4. Impact of water mobility on shear cohesion

In the previous section, we deduced that the mobility of interfacial water may be the controlling factor for shear cohesion in C-S-H. To test this conclusion, we have conducted a few additional simulations to measure how the shear strength evolves as a function of water mobility alone, without modifying neither the water content nor the interfacial distance. To alter water mobility, we have operated on two parameters: temperature and electrostatic confinement.

To analyse how temperature-induced water mobility affects the shear strength, we take as a reference the system with interfacial distance 0.2 nm. We repeat the same simulations previously used to compute shear strength (see the section on Computational details) but this time at different temperatures, from 100 K to 400 K. Fig. 6a (blue) shows that, expectedly, higher temperatures entail higher diffusion coefficients of the interfacial water. This plot also suggests two regimes: below 300 K, when water diffusion only increases slightly with temperature, and above 300 K, when the diffusivity increases sharply. In

other words, water begins to flow at 300 K. If shear cohesion is indeed controlled by the diffusivity of the interfacial water, then the relationship between shear strength and temperature should also display a change of regime at around 300 K. This change of regime is confirmed in Fig. 6a (red), where below 300 K the shear strength progressively decreases as the temperature increases, whereas above 300 K the shear strength remains constant around a minimum value of approximately 0.15 GPa. The same value of 0.15 GPa coincides with the shear strength at the transition from water bilayer to a trilayer in Fig. 4a.

A second approach to alter the mobility of water is by changing its electrostatic confinement, which induces two different mechanisms: (i) water molecules tend to coordinate to free ions in solution forming a well-defined hydration shell that moves as a whole. The diffusion of such hydration shells in nanoconfined spaces is hindered, reducing the effective diffusivity of water; (ii) in confined regions, the orientation of the water molecules in the hydration shell can induce long-range order in other water molecules at distances greater than 1 nm [21]. Therefore, also water molecules that are further away from the ions may have reduced diffusivity. To test the effect of electrostatic confinement we added extra $\text{Ca}(\text{OH})_2$ molecules in the interlayer space of C-S-H with an interfacial distance of 0.5 nm, while the C-S-H structure and interlayer water content remain unchanged. In this way, the Ca concentration rises gradually from 7.8 M, when no extra Ca is added, up to 14.9 M. Previous work showed swelling upon calcium addition to the interlayer [76]. Here swelling was not recorded because Ca was added to rather thick (0.5 nm) interlayer spaces compared to the previous work. Fig. 6b shows that at 7.8 M (red) all Ca ions are absorbed on the C-S-H surface and no detached Ca is observed in the interlayer. As more Ca is added, the adsorption sites at the C-S-H surface saturate, and Ca ions start to populate the interlayer space. Ca atoms do not arrange in a particular order and cover evenly the whole interlayer space. Fig. 6c (blue) shows that the average water diffusivity decreases with the concentration of Ca; this is due to the electrostatic confinement. Fig. 6c (red) shows that the reduction in water diffusivity, due to the Ca in solution, corresponds to an increase in shear strength. This latter indeed goes from a negligible value at low Ca concentrations, when the flow of water is hardly hindered at all, to a much higher value at high Ca concentrations, comparable with the shear strength of systems with interfaces less than 0.2 nm wide, when extra Ca was not added (see Fig. 4a). This result highlights the impact that interlayer ion concentrations may have on the mechanical performance of the material.

4. Conclusions

In this work, we investigate the mechanisms of the nanometer-sized C-S-H particles to relax shear stress as a function of the interfacial distance by performing molecular dynamics simulations. For an ideal interface under a constant shear strain applied parallel to the interlayer space, the maximum shear strength of 0.72 GPa is reached at a strain of about 12.5%. Then, as the interfacial distance increase, the shear

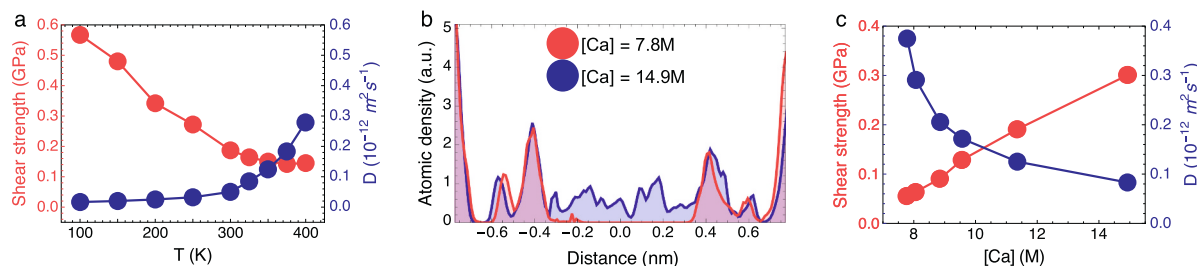


Fig. 6. (a) Average diffusion coefficients of water (in blue) and shear strength of the C-S-H systems (in red) as functions of the temperature. (b) Atomic density profiles of Ca for C-S-H samples with Ca concentrations of 7.8 M and 14.9 M. (c) Average diffusion coefficients of water (in blue) and shear strength of the C-S-H systems (in red) as functions of Ca concentration in the interlayer space. (For interpretation of the references to colour in this figure legend, the reader is referred to the web version of this article.)

strength drops drastically, suggesting that the cohesion between particles under shear is lost at interfacial distances larger than 0.3 nm.

The spatial distribution of the local shear strain reveals that the interlayer space is responsible for the stress dissipation, whereas the C-S-H layers do not participate in the relaxation, indicating that the relaxation takes place by sliding adjacent layers over each other through the interlayer space, in a so-called *stick-slip* relaxation mechanism. In this way, the cohesion between layers can be related to the interfacial distance and its water content. The analysis of the water properties shows that water begins to flow at interfacial distances above 0.3 nm, matching with the transition from water bilayer to water trilayer and the observed lost cohesion. This suggests that water mobility is the origin of the decrease of shear strength.

Finally, we analyse the evolution of the shear strength as a function of water mobility for a given interfacial distance and water content. Water mobility is altered by modifying temperature and electrostatic confinement in the interlayer space. In both cases, we observed that when water mobility is increased by raising the temperature or decreasing the ionic strength, the shear strength is reduced, and as soon as water begins to flow, the shear strength reaches very low values. This confirms that the shear cohesion in C-S-H gel is controlled by the mobility of the interlayer water.

CRedit authorship contribution statement

Eduardo Duque-Redondo: Formal analysis, Investigation, Writing-Original draft preparation.

Enrico Masoero: Methodology, Conceptualization, Writing-Reviewing and Editing, Supervision.

Hegoi Manzano: Methodology, Conceptualization, Writing-Reviewing and Editing, Supervision, Project administration.

Declaration of competing interest

The authors declare that they have no known competing financial interests or personal relationships that could have appeared to influence the work reported in this paper.

Acknowledgements

We gratefully acknowledge the financial support by “Departamento de Educación, Política Lingüística y Cultura del Gobierno Vasco” (IT912-16, IT1639-22). E.D.-R. acknowledges the postdoctoral fellowship from “Programa Posdoctoral de Perfeccionamiento de Personal Investigador Doctor” of the Basque Government. The authors thank for technical and human support provided by i2basque and SGiker (UPV/EHU/ERDF, EU), for the allocation of computational resources provided by the Scientific Computing Service.

Appendix A. Supplementary data

Supplementary data to this article can be found online at <https://doi.org/10.1016/j.cemconres.2022.106716>.

References

- [1] K. Ioannidou, K.J. Krakowiak, M. Bauchy, C.G. Hoover, E. Masoero, S. Yip, F.-J. Ulm, P. Levitz, R.J.-M. Pellenq, E. Del Gado, Mesoscale texture of cement hydrates, *Proc. Natl. Acad. Sci.* 113 (2016) 2029–2034.
- [2] H.M. Jennings, Refinements to colloid model of CSH in cement: CM-II, *Cem. Concr. Res.* 38 (2008) 275–289.
- [3] G. Constantinides, F.-J.J. Ulm, The nanogranular nature of C-S-H, *J. Mech. Phys. Solids* 55 (2007) 64–90.
- [4] M. Vandamme, F.-J.J. Ulm, Nanogranular origin of concrete creep, *Proc. Natl. Acad. Sci. U. S. A.* 106 (2009) 10552–10557, <https://doi.org/10.1073/pnas.0901033106>.
- [5] Z.P. Bazant, A.B. Høgggaard, S. Baweja, F.-J. Ulm, Microprestress-solidification theory for concrete creep. I: aging and drying effects, *J. Eng. Mech.* 123 (1997) 1188–1194.
- [6] E. Masoero, G. Di Luzio, Nanoparticle simulations of logarithmic creep and microprestress relaxation in concrete and other disordered solids, *Cem. Concr. Res.* 137 (2020), 106181.
- [7] K. Ioannidou, E. Del Gado, F.-J. Ulm, R.J.-M. Pellenq, Inhomogeneity in cement hydrates: linking local packing to local pressure, *J. Nanomech. Micromech.* 7 (2017) 4017003.
- [8] H. Liu, S. Dong, L. Tang, N.M.A. Krishnan, G. Sant, M. Bauchy, Effects of polydispersity and disorder on the mechanical properties of hydrated silicate gels, *J. Mech. Phys. Solids* 122 (2019) 555–565.
- [9] A. Morshedifard, S. Masoumi, M.J.A. Qomi, Nanoscale origins of creep in calcium silicate hydrates, *Nat. Commun.* 9 (2018) 1–10.
- [10] H. Manzano, E. Masoero, I. Lopez-Arbeloa, H.M. Jennings, Shear deformations in calcium silicate hydrates, *Soft Matter* 9 (2013) 7333–7341, <https://doi.org/10.1039/C3SM50442E>.
- [11] H. Ye, Creep mechanisms of calcium-silicate-hydrate: an overview of recent advances and challenges, *Int. J. Concr. Struct. Mater.* 9 (2015) 453–462.
- [12] M. Haist, T. Divoux, K.J. Krakowiak, J. Skibsted, R.J.-M. Pellenq, H.S. Müller, F.-J. Ulm, Creep in reactive colloidal gels: a nanomechanical study of cement hydrates, 2020. *ArXiv Prepr. ArXiv2008.02617*.
- [13] W.-S. Chiang, E. Fratini, P. Baglioni, D. Liu, S.-H. Chen, Microstructure determination of calcium-silicate-hydrate globules by small-angle neutron scattering, *J. Phys. Chem. C* 116 (2012) 5055–5061, <https://doi.org/10.1021/jp300745g>.
- [14] L.B. Skinner, S.R. Chae, C.J. Benmore, H.R. Wenk, P.J.M. Monteiro, Nanostructure of calcium silicate hydrates in cements, *Phys. Rev. Lett.* 104 (2010) 195502, 1–195502, <https://doi.org/10.1103/PhysRevLett.104.195502>.
- [15] A. Ayuela, J.S. Dolado, I. Campillo, Y.R. De Miguel, E. Erkizia, D. Sánchez-Portal, A. Rubio, A. Porro, P.M. Echenique, Silicate chain formation in the nanostructure of cement-based materials, *J. Chem. Phys.* 127 (2007), 164710.
- [16] S.M. Auerbach, K.A. Carrado, P.K. Dutta, *Handbook of Layered Materials*, New York, 2004. doi:ISBN: 0-8247-5349-6.
- [17] D.G. Evans, R.C.T. Slade, Structural aspects of layered double hydroxides, in: *Layer. Double Hydroxides*, Springer, 2006, pp. 1–87.
- [18] D.A. Young, D.E. Smith, Simulations of clay mineral swelling and hydration: dependence upon interlayer ion size and charge, *J. Phys. Chem. B* 104 (2000) 9163–9170.
- [19] P. Sellin, O.X. Leupin, The use of clay as an engineered barrier in radioactive-waste management—a review, *Clay Clay Miner.* 61 (2013) 477–498.
- [20] P.A.P.A. Bonnaud, H. Manzano, R. Miura, A.A. Suzuki, N. Miyamoto, N. Hatakeyama, A. Miyamoto, Temperature dependence of nanoconfined water properties: application to cementitious materials, *J. Phys. Chem. C* 120 (2016) 11465–11480, <https://doi.org/10.1021/acs.jpcc.6b00944>.
- [21] M. Youssef, R.J.M. Pellenq, B. Yildiz, Glassy nature of water in an ultraconfining disordered material: the case of calcium-silicate-hydrate, *J. Am. Chem. Soc.* 133 (2011) 2499–2510, <https://doi.org/10.1021/ja107003a>.
- [22] R. Alizadeh, J.J. Beaudoin, L. Raki, Viscoelastic nature of calcium silicate hydrate, *Cem. Concr. Compos.* 32 (2010) 369–376.
- [23] P. Suwanmaneechot, A. Aili, I. Maruyama, Creep behavior of CSH under different drying relative humidities: interpretation of microindentation tests and sorption measurements by multi-scale analysis, *Cem. Concr. Res.* 132 (2020), 106036.
- [24] D.W. Gardner, J. Li, M. Kunz, C. Zhu, P.J.M. Monteiro, R. Maboudian, C. Carraro, Plastic deformation mechanism of calcium-silicate hydrates determined by deviatoric-stress raman spectroscopy, *Cem. Concr. Res.* 146 (2021), 106476.
- [25] J. Li, W. Zhang, P.J.M. Monteiro, Preferred orientation of calcium aluminosilicate hydrate compacts: implications for creep and indentation, *Cem. Concr. Res.* 143 (2021), 106371.
- [26] G. Geng, R.N. Vasin, J. Li, M.J.A. Qomi, J. Yan, H.-R. Wenk, P.J.M. Monteiro, Preferred orientation of calcium aluminosilicate hydrate induced by confined compression, *Cem. Concr. Res.* 113 (2018) 186–196.
- [27] I. Maruyama, T. Ohkubo, T. Haji, R. Kurihara, Dynamic microstructural evolution of hardened cement paste during first drying monitored by ¹H NMR relaxometry, *Cem. Concr. Res.* 122 (2019) 107–117.
- [28] R. Dupuis, J. Moon, Y. Jeong, R. Taylor, S.-H. Kang, H. Manzano, A. Ayuela, P.J. M. Monteiro, J.S. Dolado, Normal and anomalous self-healing mechanism of crystalline calcium silicate hydrates, *Cem. Concr. Res.* 142 (2021), 106356.
- [29] F. Lolli, H. Manzano, J.L. Provis, M.C. Bigozzi, E. Masoero, Atomistic simulations of geopolymer models: the impact of disorder on structure and mechanics, *ACS Appl. Mater. Interfaces* 10 (2018) 22809–22820.
- [30] S.D. Palkovic, S. Moeini, S. Yip, O. Büyüköztürk, Mechanical behavior of a composite interface: calcium-silicate-hydrates, *J. Appl. Phys.* 118 (2015), 034305, <https://doi.org/10.1063/1.4926870>.
- [31] R.F. Feldman, P.J. Sereda, A new model for hydrated Portland cement and its practical implications, *Eng. J.* 53 (1970) 53–59.
- [32] M.F. Kai, L.W. Zhang, K.M. Liew, New insights into creep characteristics of calcium silicate hydrates at molecular level, *Cem. Concr. Res.* 142 (2021), 106366.
- [33] A.C.A. Muller, K.L. Scrivener, A.M. Gajewicz, P.J. McDonald, Use of bench-top NMR to measure the density, composition and desorption isotherm of C-S-H in cement paste, *Microporous Mesoporous Mater.* 178 (2013) 99–103, <https://doi.org/10.1016/j.micromeso.2013.01.032>.
- [34] M.B. Pinson, E. Masoero, P.A. Bonnaud, H. Manzano, Q. Ji, S. Yip, J.J. Thomas, M. Z. Bazant, K.J. Van Vliet, H.M. Jennings, Hysteresis from multiscale porosity: modeling water sorption and shrinkage in cement paste, *Phys. Rev. Appl.* 3 (2015) 64009, 1–64009, 17.
- [35] P.A. Bonnaud, C. Labbez, R. Miura, A. Suzuki, N. Miyamoto, N. Hatakeyama, A. Miyamoto, K.J. Van Vliet, Interaction grand potential between

- calcium-silicate-hydrate nanoparticles at the molecular level, *Nanoscale* 8 (2016) 4160–4172.
- [36] E. Masoero, E. Del Gado, R.-M. Pellenq, F.-J. Ulm, S. Yip, Nanostructure and nanomechanics of cement: polydisperse colloidal packing, *Phys. Rev. Lett.* 109 (2012), 155503.
- [37] G. Kovacević, L. Nicoleau, A. Nonat, V. Veryazov, Revised atomistic models of the crystal structure of C-S-H with high C/S ratio, <sb:contribution><sb:title>Z. Phys.</sb:title></sb:contribution><sb:host><sb:issue><sb:series><sb:title>Chem.</sb:title></sb:series></sb:issue></sb:host> 230 (2016) 1411–1424.
- [38] R.J.-M.M. Pellenq, A. Kushima, R. Shahsavari, K.J. Van Vliet, M.J. Buehler, S. Yip, F.-J. Ulm, A realistic molecular model of cement hydrates, *Proc. Natl. Acad. Sci. U. S. A.* 106 (2009) 16102–16107.
- [39] M.J. Abdolhosseini Qomi, K.J. Krakowiak, M. Bauchy, K.L. Stewart, R. Shahsavari, D. Jagannathan, D.B. Brommer, A. Baronnet, M.J. Buehler, S. Yip, F.-J. Ulm, K. J. Van Vliet, R.J.M. Pellenq, M.J.A. Qomi, K.J. Krakowiak, M. Bauchy, K.L. Stewart, R. Shahsavari, D. Jagannathan, D.B. Brommer, A. Baronnet, M.J. Buehler, S. Yip, Combinatorial molecular optimization of cement hydrates, *Nat. Commun.* 5 (2014) 1–10, <https://doi.org/10.1038/ncomms5960>.
- [40] A. Nonat, The structure and stoichiometry of CSH, *Cem. Concr. Res.* 34 (2004) 1521–1528.
- [41] S. Garrault, E. Finot, E. Lesniewska, A. Nonat, Study of CSH growth on C 3 S surface during its early hydration, *Mater. Struct.* 38 (2005) 435–442.
- [42] I.G. Richardson, G.W. Groves, Microstructure and microanalysis of hardened ordinary Portland cement pastes, *J. Mater. Sci.* 28 (1993) 265–277.
- [43] J.J. Chen, J.J. Thomas, H.F.W. Taylor, H.M. Jennings, Solubility and structure of calcium silicate hydrate, *Cem. Concr. Res.* 34 (2004) 1499–1519, <https://doi.org/10.1016/j.cemconres.2004.04.034>.
- [44] A.J. Allen, J.J. Thomas, H.M. Jennings, Composition and density of nanoscale calcium-silicate-hydrate in cement, *Nat. Mater.* 6 (2007) 311–316, <https://doi.org/10.1038/nmat1871>.
- [45] A. Kumar, B.J. Walder, A. Kunhi Mohamed, A. Hofstetter, B. Srinivasan, A. J. Rossini, K. Scrivener, L. Emsley, P. Bowen, The atomic-level structure of cementitious calcium silicate hydrate, *J. Phys. Chem. C* 121 (2017) 17188–17196.
- [46] J.M. Martínez, L. Martínez, Packing optimization for automated generation of complex system's initial configurations for molecular dynamics and docking, *J. Comput. Chem.* 24 (2003) 819–825, <https://doi.org/10.1002/jcc.10216>.
- [47] S. Plimpton, Fast parallel algorithms for short-range molecular dynamics, *J. Comput. Phys.* 117 (1995) 1–19, <https://doi.org/10.1006/jcph.1995.1039>.
- [48] H. Manzano, R.J.M. Pellenq, F.-J. Ulm, M.J. Buehler, A.C.T. van Duin, Hydration of calcium oxide surface predicted by reactive force field molecular dynamics, *Langmuir* 28 (2012) 4187–4197, <https://doi.org/10.1021/la204338m>.
- [49] H. Manzano, S. Moeni, F. Marinelli, A.C.T. van Duin, F.-J. Ulm, R.J.M. Pellenq, Confined water dissociation in microporous defective silicates: mechanism, dipole distribution, and impact on substrate properties, *J. Am. Chem. Soc.* 134 (2012) 2208–2215, <https://doi.org/10.1021/ja209152n>.
- [50] D. Hou, T. Zhao, H. Ma, Z. Li, Reactive molecular simulation on water confined in the nanopores of the calcium silicate hydrate gel: structure, reactivity, and mechanical properties, *J. Phys. Chem. C* 119 (2015) 1346–1358.
- [51] M. Bauchy, H. Laubie, M.J.A. Qomi, C.G. Hoover, F.-J. Ulm, R.-M. Pellenq, Fracture toughness of calcium-silicate-hydrate from molecular dynamics simulations, *J. Non-Cryst. Solids* 419 (2015) 58–64.
- [52] M.J.A. Qomi, M. Bauchy, F.-J. Ulm, R.J.-M. Pellenq, Anomalous composition-dependent dynamics of nanoconfined water in the interlayer of disordered calcium-silicates, *J. Chem. Phys.* 140 (2014) 054515_1–054515_11, <https://doi.org/10.1063/1.4864118>.
- [53] W. Shinoda, M. Shiga, M. Mikami, Rapid estimation of elastic constants by molecular dynamics simulation under constant stress, *Phys. Rev. B* 69 (2004), 134103.
- [54] H. Grubmüller, H. Heller, A. Windemuth, K. Schulten, Generalized verlet algorithm for efficient molecular dynamics simulations with long-range interactions, *Mol. Simul.* 6 (1991) 121–142.
- [55] M. Brehm, B. Kirchner, TRAVIS - a free analyzer and visualizer for Monte Carlo and Molecular dynamics trajectories, *J. Chem. Inf. Model.* 51 (2011) 2007–2023, <https://doi.org/10.1021/ci200217w>.
- [56] M. Brehm, M. Thomas, S. Gehrke, B. Kirchner, TRAVIS—a free analyzer for trajectories from molecular simulation, *J. Chem. Phys.* 152 (2020), 164105.
- [57] A. Stukowski, Visualization and analysis of atomistic simulation data with OVITO—the Open Visualization Tool, *Model. Simul. Mater. Sci. Eng.* 18 (2009) 015012_1–015012_7.
- [58] C.P. Morrow, A.Ö. Yazaydin, M. Krishnan, G.M. Bowers, A.G. Kalinichev, R. J. Kirkpatrick, Structure, energetics, and dynamics of smectite clay interlayer hydration: molecular dynamics and metadynamics investigation of Na-hectorite, *J. Phys. Chem. C* 117 (2013) 5172–5187, <https://doi.org/10.1021/jp312286g>.
- [59] E. Duque-Redondo, I. López-Arbeloa, H. Manzano, Distinctive diffusion regimes of organic molecules in clays: (de)coupled motion with water, *J. Phys. Chem. C* 123 (2018) 511–516, <https://doi.org/10.1021/acs.jpcc.8b09639>.
- [60] S. Masoumi, H. Valipour, M.J. Abdolhosseini Qomi, Intermolecular forces between nanolayers of crystalline calcium-silicate-hydrates in aqueous medium, *J. Phys. Chem. C* 121 (2017) 5565–5572.
- [61] L.D. Gelb, K.E. Gubbins, Characterization of porous glasses: a simulation models, adsorption isotherms, and the Brunauer–Emmett–Teller analysis method, *Langmuir* 14 (1998) 2097–2111, <https://doi.org/10.1021/la9710379>.
- [62] E. Okabe, B. Boots, K. Sugihara, S.N. Chiu, D.G. Kendall, *Spatial Tessellations: Concepts And Applications of Voronoi Diagrams*, Second Edition, Wiley Online Library, 2000.
- [63] H. Manzano, E. Duque-Redondo, E. Masoero, I. López-Arbeloa, The role of water on CSH gel shear strength studied by molecular dynamics simulations, in: *CONCREEP* 10, 2015, pp. 899–907, <https://doi.org/10.1061/9780784479346.107>.
- [64] B. Carrier, M. Vandamme, R.J.-M. Pellenq, H. Van Damme, Elastic properties of swelling clay particles at finite temperature upon hydration, *J. Phys. Chem. C* 118 (2014) 8933–8943.
- [65] F.-J. Ulm, M. Vandamme, C. Bobko, J. Alberto Ortega, K. Tai, C. Ortiz, Statistical indentation techniques for hydrated nanocomposites: concrete, bone, and shale, *J. Am. Ceram. Soc.* 90 (2007) 2677–2692, <https://doi.org/10.1111/j.1551-2916.2007.02012.x>.
- [66] G. Hantal, L. Brochard, H. Laubie, D. Ebrahimi, R.J.-M. Pellenq, F.-J. Ulm, B. Coasne, Atomic-scale modelling of elastic and failure properties of clays, *Mol. Phys.* 112 (2014) 1294–1305.
- [67] B. Bhushan, J.N. Israelachvili, U. Landman, Nanotribology: friction, wear and lubrication at the atomic scale, *Nature* 374 (1995) 607–616.
- [68] E. Duque-Redondo, H. Manzano, N. Epelde-Elezcano, V. Martínez-Martínez, I. López-Arbeloa, Molecular forces governing shear and tensile failure in clay-dye hybrid materials, *Chem. Mater.* 26 (2014) 4338–4345, <https://doi.org/10.1021/cm500661d>.
- [69] D. Hou, Y. Zhu, Y. Lu, Z. Li, Mechanical properties of calcium silicate hydrate (C-S-H) at nano-scale: a molecular dynamics study, *Mater. Chem. Phys.* 146 (2014) 503–511.
- [70] D. Fan, S. Yang, Mechanical properties of CSH globules and interfaces by molecular dynamics simulation, *Constr. Build. Mater.* 176 (2018) 573–582.
- [71] A.G. Kalinichev, J.W. Wang, R.J. Kirkpatrick, Molecular dynamics modeling of the structure, dynamics and energetics of mineral-water interfaces: application to cement materials, *Cem. Concr. Res.* 37 (2007) 337–347, <https://doi.org/10.1016/j.cemconres.2006.07.004>.
- [72] H. Manzano, W. Zhang, M. Raju, J.S. Dolado, I. López-Arbeloa, A.C.T. van Duin, Benchmark of ReaxFF force field for subcritical and supercritical water, *J. Chem. Phys.* 148 (2018), 234503.
- [73] P.A. Netz, F.W. Starr, M.C. Barbosa, H.E. Stanley, Relation between structural and dynamical anomalies in supercooled water, *Phys. A Stat. Mech. Appl.* 314 (2002) 470–476.
- [74] R. Laenen, C. Rauscher, A. Laubereau, Dynamics of local substructures in water observed by ultrafast infrared hole burning, *Phys. Rev. Lett.* 80 (1998) 2622.
- [75] C.J. Fecko, J.D. Eaves, J.J. Loparo, A. Tokmakoff, P.L. Geissler, Ultrafast hydrogen-bond dynamics in the infrared spectroscopy of water, *Science* (80-.) 301 (2003) 1698–1702.
- [76] M.J.A. Qomi, L. Brochard, T. Honorio, I. Maruyama, M. Vandamme, Advances in atomistic modeling and understanding of drying shrinkage in cementitious materials, *Cem. Concr. Res.* 148 (2021), 106536.